9-1-2013

Thermodynamic Characterization of Five Key Kinetic Parameters That Define Neuronal Nitric Oxide Synthase Catalysis

Mohammad Mahfuzul Haque
Lerner Research Institute

Jesus Tejero
Lerner Research Institute

Mekki Bayachou
Cleveland State University, M.BAYACHOU@csuohio.edu

Zhi-Qiang Wang
Lerner Research Institute

Mohammed Fadlalla
Lerner Research Institute

See next page for additional authors

Publisher's Statement

This is the accepted version of the following article: http://onlinelibrary.wiley.com/doi/10.1111/febs.12404/abstract, which has been published in final form at http://onlinelibrary.wiley.com/doi/10.1111/febs.12404/abstract

Thermodynamic characterization of five key kinetic parameters that define neuronal nitric oxide synthase catalysis

Mohammad Mahfuzul Haque, Jesús Tejero, Mekki Bayachou, Zhi-Qiang Wang, Mohammed Fadlalla and Dennis J. Stuehr

Keywords
electron transfer; heme protein; heme reduction; nitric oxide synthase; stopped flow

NO synthase (NOS) enzymes convert L-arginine to NO in two sequential reactions whose rates (k_{cat1} and k_{cat2}) are both limited by the rate of ferric heme reduction (k_r). An enzyme ferric heme NO complex forms as an immediate product complex and then undergoes either dissociation (at a rate that we denote as k_d) to release NO in a productive manner, or reduction (k_r) to form a ferrous heme NO complex that must react with O_2 (at a rate that we denote as k_{ox}) in a NO dioxygenase reaction that regenerates the ferric enzyme. The interplay of these five kinetic parameters (k_{cat1}, k_{cat2}, k_r, k_d and k_{ox}) determines NOS specific activity, O_2 concentration response, and pulsatile versus steady-state NO generation. In the present study, we utilized stopped-flow spectroscopy and single catalytic turnover methods to characterize the individual temperature dependencies of the five kinetic parameters of rat neuronal NOS. We then incorporated the measured kinetic values into computer simulations of the neuronal NOS reaction using a global kinetic model to comprehensively model its temperature-dependent catalytic behaviours. The results obtained provide new mechanistic insights and also reveal that the different temperature dependencies of the five kinetic parameters significantly alter neuronal NOS catalytic behaviours and NO release efficiency as a function of temperature.

Introduction

Nitric oxide (NO) is a biological mediator produced in animals by three NO synthase isozymes (NOS; EC 1.14.13.39): inducible NOS (iNOS), neuronal NOS (nNOS) and endothelial NOS (eNOS) [1,2]. NOS enzymes catalyze a stepwise oxidation of L-arginine (Arg) to form nitric oxide and citrulline [3 5]. In the first reaction, Arg is hydroxylated to form N^{ω}-hydroxy-L-arginine (NOHA) and, in the second reaction, the NOHA intermediate is oxidized to form NO and citrulline (Scheme 1) [1]. Both steps consume one molecule of O_2 and utilize NADPH-derived reducing equivalents. NOS proteins comprise an N-terminal oxygenase domain and a C-terminal flavoprotein domain, with a calmodulin (CaM)-binding site connecting the two domains [6], and each NOS is only active as a homodimer [6,7]. The oxygenase domain binds Fe protoporphyrin IX (heme), the substrate Arg and the essential cofactor (6*R*)-tetrahydrobiopterin (H_4B) [8,9], whereas the flavoprotein domain binds FAD, FMN and NADPH [10 12]. During catalysis, the flavoprotein domain provides electrons to the heme in the NOS oxygenase domain, which enables the heme to bind O_2 and initiate oxygen activation in both reactions of NO synthesis [13 15]. Heme reduction also requires that CaM be bound to NOS, and is rate-limiting for the NO biosynthetic steps.

NOS enzymes operate under the constraint of being heme proteins that generate NO, a good heme-binding ligand. Indeed, their newly-made NO binds to the ferric heme many times before it can exit the enzyme [16]. How this intrinsic heme-NO-binding event impacts NOS catalytic cycling is shown in Fig. 1 and has been discussed in detail previously [16 20]. The Arg to NO biosynthetic reactions [Fe^{III} to ferric heme NO complex ($Fe^{III}NO$) steps in Fig. 1] involve two sequential oxidation reactions whose rates are both limited by the rate of ferric heme reduction (k_r) because all subsequent catalytic steps in either reaction (termed k_{cat1} and k_{cat2} in Fig. 1) occur faster than k_r. Once the $Fe^{III}NO$ product complex forms in NOS, it can either dissociate and enable the release of NO into the medium (at a rate k_d as shown in Fig. 1) or

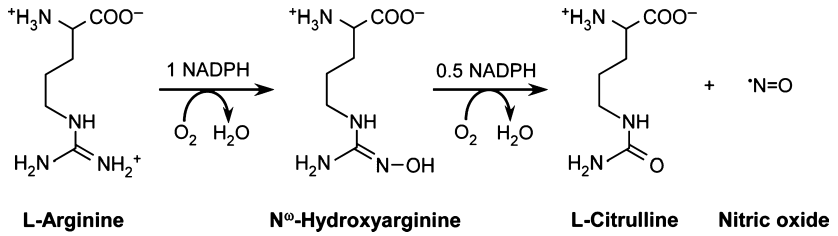

Scheme 1. Biosynthesis of nitric oxide from L arginine.

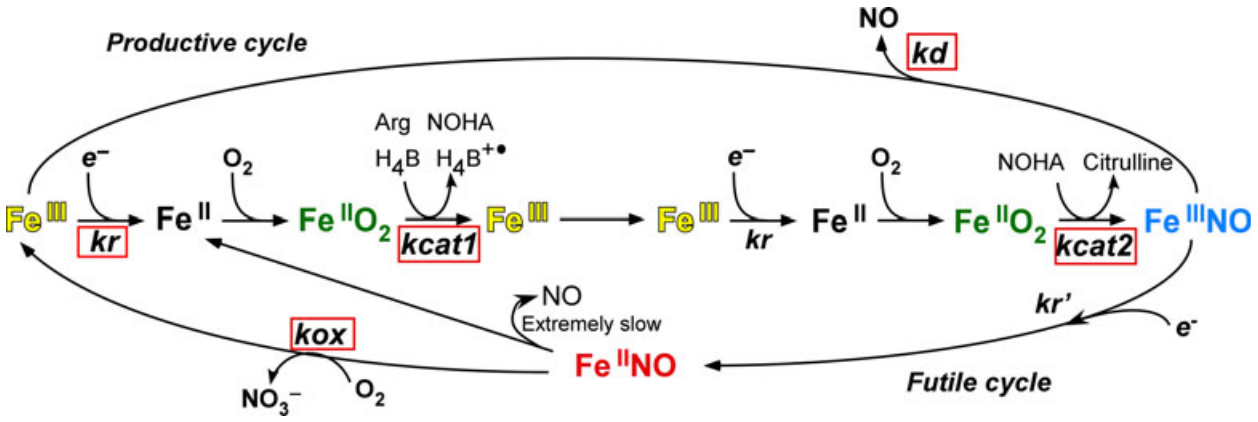

Fig. 1. Global kinetic model for NOS catalysis. NOS enzymes start with their heme in the ferric state (left side, yellow Fe^{III}). The FMN to heme electron transfers (ETs) (designated k_r) allow O_2 to bind to heme to start catalysis, and are rate limiting for the two sequential oxidation reactions (horizontal line). k_{cat1} and k_{cat2} are the conversion rates of the enzyme $Fe^{II}O_2$ species (green) to products in the L Arg and N^{ω} hydroxy L arginine (NOHA) oxidation reactions, respectively. A $Fe^{III}NO$ product complex ($Fe^{III}NO$, blue) can either release NO (k_d) or become reduced (k_r') to a $Fe^{II}NO$ complex ($Fe^{II}NO$, red), which reacts with O_2 (k_{ox}) to regenerate ferric enzyme through a futile cycle that destroys the NO. The five kinetic parameters and reactions that we studied are indicated by the red boxes.

become reduced by the flavoprotein domain (at a rate k_r' in Fig. 1; assumed to be equal to k_r) [21] to form the enzyme ferrous heme NO species ($Fe^{II}NO$), which releases NO extremely slowly [18,19]. Consequently, the $Fe^{II}NO$ species must undergo reaction with O_2 at a rate k_{ox} (Fig. 1) to regenerate the ferric enzyme and return to an active form. Thus, two cycles exist during steady state NO synthesis (Fig. 1): NO dissociation from the enzyme (k_d) is part of a 'productive cycle' that is essential for NOS bioactivity, whereas reduction of the $Fe^{III}NO$ product complex (k_r') channels NOS into a 'futile cycle' that actually represents a NO dioxygenase activity. The rate constants for each step of NOS catalysis are shown in Fig. S1.

Observed rates for k_r, k_{cat}, k_d and k_{ox} have been measured in NOS enzymes in single catalytic turnover reactions [14,18,19,22 25]. However, because most of the measures have been obtained at only a single temperature (10 °C, or less often at 25 °C), little or nothing is understood regarding the temperature dependencies and thermodynamic properties of the individual steps, as well as how they combine to govern the catalytic behaviour and overall activities of NOS enzymes. This information would improve our understanding NOS catalysis and enable the accurate modelling of its catalytic cycle under physiological temperatures and conditions. In the present study, we poised rat nNOS at different points in the cycle, and utilized stopped-flow spectroscopy to characterize the temperature dependence of five individual kinetic parameters (k_r, k_{cat1}, k_{cat2}, k_d and k_{ox}). The thermodynamic parameters of these individual reactions provide new insights regarding NOS structure reactivity relationships and provide a better understanding of their physiological relevance.

Results and Discussion

Temperature dependence of heme reduction (k_r)

We directly assessed electron transfer (ET) from FMN hydroquinone to heme using stopped-flow spectroscopy under anaerobic conditions. Heme reduction was monitored via the formation of the $Fe^{II}CO$ complex at 444 nm. Once ferrous heme is formed by ET from the FMN, the fast and stable binding of CO prevents the accumulation of the ferrous species and makes the ET reaction essentially irreversible. This mimics the normal condition of having O_2 present to react with ferrous heme, and insures that the observed rate of heme reduction does not have a significant back reaction component. The reactions were initiated by mixing CaM-bound nNOS with excess NADPH [26], and heme reduction rates (k_r) were measured at 5, 10, 15, 20, 25, 30 and 37 °C. Representative diode array spectra (Fig. 2, upper panel) and the resulting kinetic trace (Fig. 2, upper panel inset) are shown. We fit the kinetic traces to a bi-exponential function, with the initial fast phase representing an absorbance decrease as a result of flavin reduction by NADPH, and the subsequent slower phase representing the absorbance increase as a result of heme reduction in the presence of CO. The observed rates obtained for heme reduction at each temperature are provided in Table 1. The heme reduction rate increased approximately 1.5-fold with every 10 °C rise in temperature. Fitting the experimental data to the linearized form of the Arrhenius equation yielded an activation energy of E_a = 31.5 kJ·mol^{-1}. A linear Eyring plot (Fig. 2, middle panel) of the data yielded values for the enthalpy and entropy of activation for the heme reduction step: $\Delta H^{\ddagger}$ =+29.1 kJ·mol^{-1}; $\Delta S^{\ddagger}$ = −128 J·mol^{-1}·K^{-1} (Table 2). The derived Gibbs free energy of activation $\Delta G^{\ddagger}$ at 25 °C was calculated as 67.2 kJ·mol^{-1}. The $\Delta G^{\ddagger}$ increases with temperature, which is expected, given the negative entropic contribution. The activation enthalpy and entropy values for heme reduction that we determined for nNOS are similar to values recently reported for human iNOS (36.9 kJ·mol^{-1} and −89.7 J·mol^{-1}·K^{-1}, respectively), which were derived using a different measurement method (flash photolysis) [27]. This suggests that similar mechanisms may govern heme reduction among NOS isozymes.

Table 1. Measured rates (mean ± SD) at different temperatures.

Temperature (°C)	k_r (s ^{1})	k_{cat1} (s ^{1})	k_{cat2} (s ^{1})	k_d (s ^{1})	k_{ox} (s ^{1})[a]	NO synthesis (s ^{1})
5	4.2 ± 0.3	9.2 ± 0.8	16.4 ± 1.9	1.6 ± 0.2	0.063 ± 0.002	0.12 ± 0.01
10	5.3 ± 0.2	13. 5 ± 1.3	29 ± 3	3.7 ± 0.3	0.081 ± 0.005	0.27 ± 0.02
15	6.5 ± 0.4	21 ± 2	52 ± 5	5.9 ± 0.2	0.102 ± 0.002	0.35 ± 0.03
20	8.1 ± 0.6	31 ± 3	93 ± 4	10.7 ± 0.1	0.130 ± 0.001	0.55 ± 0.05
25	10.4 ± 0.5	46 ± 3	162 ± 15	20.1 ± 1.5	0.161 ± 0.003	0.82 ± 0.04
30	12.7 ± 1.1	68 ± 5	278 ± 18	31 ± 1	0.211 ± 0.004	1.12 ± 0.10
37	17.2 ± 0.6	113 ± 9	572 ± 36	58 ± 6	0.254 ± 0.002	1.40 ± 0.08

[a] Determined at approximately 202 μM O_2, 180 μM O_2, 162 μM O_2, 145 μM O_2, 135 μM O_2, 125 μM O_2 and 108 μM O_2 at 5, 10, 15, 20, 25, 30 and 37 °C, respectively (i.e. half air saturated concentration at the respective temperature).

Activation parameters of heme reduction have been determined for other heme proteins, such as azurin, cytochrome *c* oxidase and cd_1 nitrite reductase [28 31]. Particularly, activation parameters determined for interprotein ET reactions, such as in cytochrome *c*-plastocyanin [32 34], indicate modest enthalpies and high negative entropies, similar to the values that we found for nNOS with respect to its putative inter-domain FMN-to-heme ET. The high negative activation entropy determined for nNOS suggests that the rate-limiting elementary step of the heme reduction process is characterized by a relatively ordered transition state.

Table 2. Thermodynamic parameters for k_r, k_{ox}, k_d, NO synthesis, k_{cat1} and k_{cat2}. Errors indicate the SD obtained from at least three measurements. E_a values are calculated from an Arrhenius plot.

Reaction	E_a (kJ·mol ^{1})	$\Delta H^{\ddagger}$ (kJ·mol ^{1})	$\Delta S^{\ddagger}$ (J.mol ^{1}·K ^{1})
k_r	31.5 ± 0.5	29.1 ± 0.5	128 ± 3
k_{cat1}	57.1 ± 2.3	54.7 ± 2.3	29 ± 1
k_{cat2}	79.5 ± 2.7	77 ± 3	+56 ± 2
k_d	83.1 ± 1.7	80.7 ± 1.7	+50 ± 1
k_{ox}	31.9 ± 1.0	29.4 ± 1.0	161 ± 14
NO synthesis	54.1 4.5	51.7 4.5	74 9

Because heme reduction in nNOS involves an ET reaction between the FMN and heme prosthetic groups, we analyzed the temperature dependence data of heme reduction in the framework of the semi-classical Marcus theory describing nonadiabatic ET reactions [35]. This approach has been successfully applied to several biological ET systems to shed light on quantitative aspects of the ET step [36,37]. It is important to note that heme reduction in NOS enzymes is a relatively complex multistep process. A protein conformational change that involves both long- and short-range motions is expected to bring the FMN domain into close proximity to the heme centre in the oxygenase domain of the nitric oxide synthase (NOSoxy) [38,39]. Mutational and kinetic studies suggest that the FMN domain first undergoes a long

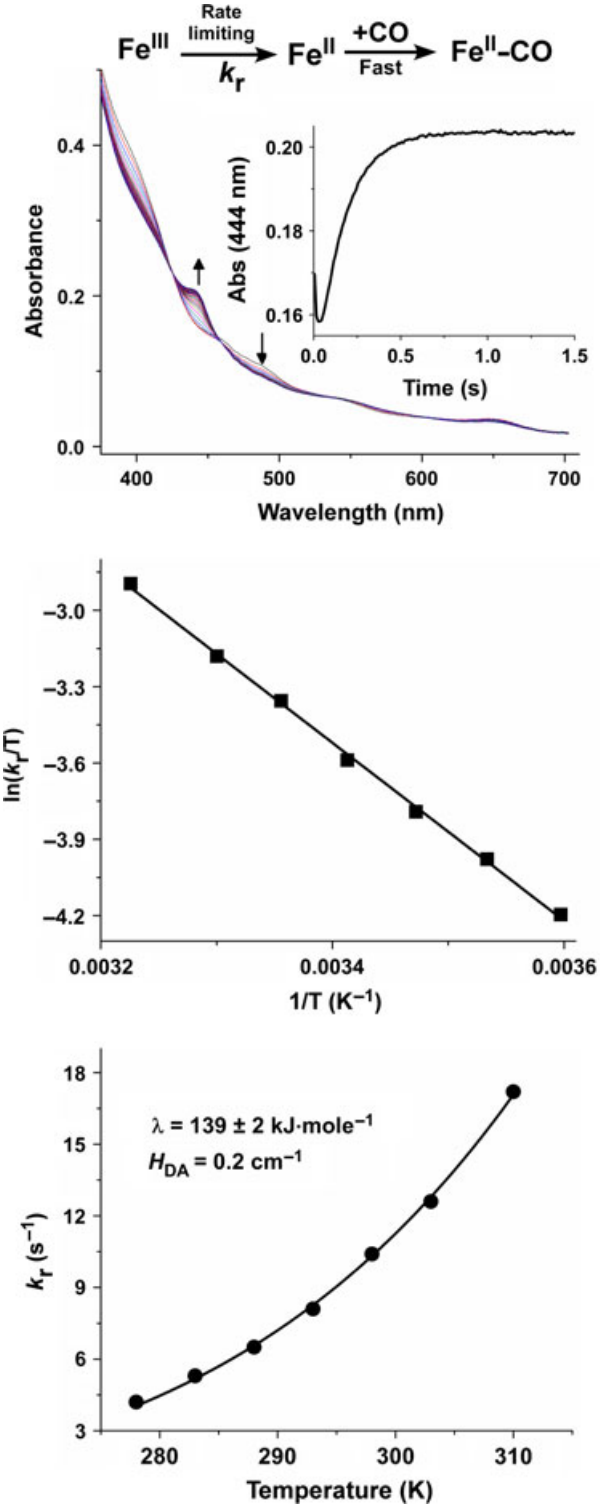

Fig. 2. Temperature dependence of ferric heme reduction (k_r) in nNOS. Anaerobic ferric nNOS (~ 10 μM) was mixed at various temperatures with NADPH (100 μM) in CO saturated buffer in the stopped flow apparatus and build up of the $Fe^{II}CO$ absorbance peak (444 nm) was used to measure the rate of heme reduction. Upper panel: rapid scanning spectra recorded during a representative reaction run at 10 °C and the accompanying kinetics of spectral change (inset). Middle panel: Eyring plot of the measured heme reduction rates, with slope $\Delta H^{\ddagger}/R$ and the intercept $\Delta S^{\ddagger}/R + \ln(k_B/h)$. Lower panel: temperature dependence of the nNOS heme reduction rate in the context of the Marcus ET theory. The solid line represents a nonlinear least squares fit of the data using Equation (1) as described in the text. The derived Marcus parameters (λ and H_{DA}) giving the best fit are shown.

range motion to swing away from the ferredoxin NADP-reductase (FNR) domain and then undergoes short-range sampling motions to productively dock on the NOSoxy domain, which is in part guided by complementary charged residues on the domain domain interface [11,39 41]. These conformational change(s) precede the actual ET and could conceivably influence the kinetics and thermodynamic behaviour of the heme reduction that we observe. The ET process would be gated if the conformational change is rate-limiting, whereas, if the actual FMN-to-heme ET step is rate-limiting, the process could be either true-ET or coupled-ET. In true-ET, the ET step is rate-limiting and not kinetically influenced by preceding steps, whereas, in coupled-ET, the ET reaction is still rate-limiting but is preceded by a relatively fast and thermodynamically unfavourable non-ET reaction such as conformational change. Although the FMN to heme ET in NOS enzymes has been reported to be conformationally-gated [42], a detailed study on this aspect is lacking. Application of the Marcus ET formalism to our temperature dependence data provides an opportunity to quantify parameters such as the required reorganization energy, as well as electronic coupling between the FMN electron donor and heme electron acceptor during ET. The rate constant for nonadiabatic ET, k_{ET}, is generally described by Equations (1,2) which respectively, derive from the prediction that rates of ET exhibit Gaussian free-energy dependence, and from the fact that electronic coupling drops exponentially with distance between redox partners:

$$k_{ET} = \frac{4\pi^2 H_{AB}^2}{h(4\pi\lambda RT)^{1/2}} exp\left[-\frac{(\Delta G^\circ + \lambda)^2}{4\lambda RT}\right] \quad (1)$$

$$k_{ET} = k_0\ exp[-\beta(r - r_0)] exp\left[-\frac{(\Delta G^\circ + \lambda)^2}{4\lambda RT}\right] \quad (2)$$

where λ is the reorganization energy and ΔG° is the thermodynamic driving force determined from the redox potential difference for the redox partners (FMN and heme in this case). The other parameters have their usual meanings: h is Planck's constant; R is the gas constant; and T is absolute temperature. H_{DA} describes the electronic coupling between electron donor (FMN) and electron acceptor (heme). In Equation (2): $k_o = 10^{13}\ s^{-1}$ is the characteristic maximum limit for k_{ET} when donor and acceptor are in van der Waals' contact (i.e. at $r_o = 3$ Å) and when no activation is involved (i.e. when $\lambda = \Delta G^\circ$). The value of parameter β reflects the nature of the intervening medium in mediating the ET, and a value of 1.4 $Å^{-1}$ is widely used for proteins [36].

In Fig. 2 (lower panel), the heme reduction data as a function of temperature were fit using Equation 1 to obtain estimates of the reorganization energy (λ) and the electronic coupling element (H_{DA}). The ΔG^o value used for the fitting was -0.030 eV (or -2.9 kJ·mol^{-1}). This driving force is determined from the difference of midpoint values of the FMN hydroquinone/semiquinone couple and the heme $Fe^{III}/Fe^{II}CO$ couple in nNOS [38,43 46]. Using this ΔG^o value, the nonlinear fitting yielded best-fit values for the reorganization energy λ = 139 kJ·mol^{-1} (or ~ 1.4 eV) and an electronic coupling factor H_{DA} = 0.2 cm^{-1}. We have varied ΔG^o aiming to investigate whether the values determined by fitting are affected by the driving force used. Changes of as much as $\pm$ 60 mV in ΔG^o do not result in significant changes in the fitted values of λ or H_{DA}. Fitting the same data to Equation (2) gave a similar value for the reorganization energy λ = 135 kJ·mol^{-1} (Fig. S2, upper panel), which is not significantly different from λ =139 kJ·mol^{-1} determined using Equation (1).

The estimate for H_{DA} in nNOS is within the range known for nonadiabatic ET [35], whereas the estimated reorganization energy (λ = 1.4 eV) lies on the higher end but is still within the range of reorganizational energies reported for most physiological ET reactions (i.e. λ = 0.5 2.3 eV) [36]. The relatively high value of λ in our case reflects a possible coupling of ET to the pre-requisite conformational change needed to bring the FMN domain within a distance required for ET to the heme in the nNOSoxy. Whether an ET reaction is gated or coupled depends on the relative rates of the ET and prerequisite non-ET steps. An estimated value of K_{eq} = 9.0 was reported for the FMN FNR domain off/on conformational equilibrium for the reduced, CaM-bound nNOS at 10 °C [38], indicating that, once reduced, the FMN domain is mostly away from the FNR and thus in a conformation that could interact with nNOSoxy for ET. However, the corresponding k_{off} value associated with the FNR FMN equilibrium under this condition is not yet known and, in our experimental design, the FMN domain must first receive electrons from the FNR to become reduced. Also, the K_{eq} for the corresponding FMN NOSoxy equilibrium has been studied in the CaM-bound nNOS poised at different redox states. The data indicate a low value ($K_{eq} \leq 0.2$) [47,48] exists in all cases. This suggests that very little FMN nNOSoxy complex is present at equilibrium and that their interaction is intermittent and/or transient. Given the relatively slow rates for heme reduction that we

observe in nNOS, the relatively high corresponding reorganization energy, and the unfavourable on/off thermodynamic equilibrium for the FMN nNOSoxy interaction, ET from FMN to heme in nNOS is likely coupled to the pre-requisite conformational movement of the FMN domain. Similar ET reactions that are coupled to conformational equilibria are known. One example is the ET reaction from methanol dehydrogenase to the heme in cytochrome *c-551i* where the ET is rate-limiting but still influenced by a pre-requisite rapid but unfavourable conformational arrangement [49].

Our fit of the heme reduction versus temperature data to Equation (2) also yielded an estimate for the distance '*r*' (FMN-to-heme distance) (Fig. S2). The estimated distance at the time of the ET event is $r \approx 13.4$ Å. It is important to note that this distance does not change significantly ($r = 13.1$ Å) when the data are fit with Equation (2) using the λ value found in nonlinear fitting with Equation (1) (λ = 139 kJ·mol^{-1}) (Fig. S2, lower panel). This estimate is in excellent agreement with FMN-to-heme distances of 9 15 Å proposed based on docking models for FMN NOSoxy complexes [40,50]. The value is also consistent with the proposed range (12 13 Å) suggested for nNOS based on the kinetics of heme-to-FMN back ET determined by pulse radiolysis [42] and the recent studies on FMN heme coupling by pulsed EPR for human iNOS [51]. In this case, a distance of 18.8 Å between the FMN-N5 atom and the heme iron was determined, which could correspond to an edge to edge FMN heme distance as short as 13.1 Å [51]. Comparable distances have been reported in related flavocytochrome systems. For example, a value of 18.4 Å has been reported for the FMN to heme iron distance in the complex between the heme and FMN-binding domain of cytochrome P450BM-3 [52].

Temperature dependence of the oxygenation reactions (k_{cat1} and k_{cat2})

The k_{cat1} and k_{cat2} parameters represent the conversion rates of the heme $Fe^{II}O_2$ species to products in the Arg hydroxylation and NOHA oxidation reactions, respectively. We utilized stopped-flow spectroscopy to compare the nNOS heme transitions that occur during the single turnover reactions, as reported in previous studies [53,54]. The reactions were initiated by rapid-mixing an oxygen-containing buffer with pre-reduced ferrous nNOS proteins that contained H_4B and either Arg or NOHA as substrate. For the Arg reactions, we observed two consecutive heme transitions: $Fe^{II} \rightarrow Fe^{II}O_2 \rightarrow Fe^{III}$ and, in the reaction with NOHA, we observed three transitions: $Fe^{II} \rightarrow Fe^{II}O_2 \rightarrow Fe^{III}NO \rightarrow Fe^{III}$. Global analysis of the spectral data according to these models yielded the spectrum of each species (Fig. 3A and 3B, upper panels). The two middle panels of figure 3 show how the concentration of each species changed with time during the reactions. Linear Eyring plots of the observed rates (Fig. 3A and 3B, lower panels) show that both k_{cat1} and k_{cat2} increase as the temperature increases (Table 1) but do so according to significantly different ratios, such that the slope of k_{cat2} is 1.4-fold higher than that of k_{cat1} (Fig. 3A & 3B, lower panels). Fitting the experimental data to the Arrhenius equation yielded an activation energy $E_a = 57.1$ kJ·mol^{-1} for k_{cat1} and 79.5kJ·mol^{-1} for k_{cat2}. Linear Eyring plots give the values for the enthalpy and entropy of activation derived for k_{cat1}: $\Delta H^{\ddagger} = +54.7$ kJ·mol^{-1}; $\Delta S^{\ddagger} = -29$ J·mol^{-1}·K^{-1} (Table 2). The values for the enthalpy and entropy of activation derived for k_{cat2} are: $\Delta H^{\ddagger} = +77$ kJ·mol^{-1}; $\Delta S^{\ddagger} = +56$ J·mol^{-1}·K^{-1} (Table 2). The thermodynamic parameters derived for k_{cat1} are distinguished from k_{cat2} by a negative entropic component. The relative entropic cost observed in the first catalytic step may be attributed to the necessary change in the hydrogen-bonding network expected at the active site upon the transformation of L-arginine to the enzyme bound NOHA [55].

Temperature dependence of NO dissociation (k_d)

A variety of studies [14,25,56,57] indicate that newly-formed NO binds to the NOS ferric heme before it can exit the enzyme. This causes a $Fe^{III}NO$ product complex to form at the end of each catalytic cycle in all NOS enzymes examined to date [19]. In the NOHA single turnover reactions, there was a clear build-up of this immediate $Fe^{III}NO$ product complex (Fig. 3B, upper and middle panels), which allows us to determine the macroscopic off-rate of NO by monitoring its transition to ferric enzyme (k_d parameter in Fig. 1). The macroscopic, observed dissociation rate (k_d) of the $Fe^{III}NO$ product complex is an important parameter because it impacts NOS enzyme distribution during catalysis and, consequently, steady-state NO synthesis activity [19,23,25]. Linear Eyring plots of the observed rates (Fig. 4, upper panel and Table 1) revealed that the k_d parameter has a relatively large temperature dependence, increasing by more than three-fold every 10 °C. The thermodynamic parameters of the reaction were derived from the linear Eyring plot and Arrhenius equation, giving the values: $E_a = 83.1$ kJ·mol^{-1}; $\Delta H^{\ddagger} = 80.7$ kJ·mol^{-1}; $\Delta S^{\ddagger} = 50$ J·mol^{-1}·K^{-1} (Table 2). The activation energy for NO dissociation from Fe^{III}-nNOS (k_d) is quite close to the activation energy for citrulline

formation by nNOS as reported earlier by Iwanaga ($\simeq$103 kJ·mol^{-1}) [58]. Also, the relatively large positive activation entropy that we calculated for the k_d in nNOS is similar to values measured for NO dissociation from other ferric heme proteins such as metmyoglobin ($\Delta H^{\ddagger}$ = 78 kJ·mol^{-1}; $\Delta S^{\ddagger}$ = 46 J·mol^{-1}·K^{-1}) [59] and the camphor-bound cytochrome P450$_{cam}$ ($\Delta H^{\ddagger}$ = 84 kJ·mol^{-1}; $\Delta S^{\ddagger}$ = 41 J·mol^{-1}·K^{-1}) [60]. Overall, the process of NO release from ferric heme in nNOS exhibits similar thermodynamic behaviour to that of other heme proteins [59,60] as indicated by comparing Eyring plots for NO release data for the different heme proteins across a range of temperatures (Fig. 4, lower panel). Their similar thermodynamic behaviours are indicative of a common mechanism regulating NO dissociation from the ferric heme and its escape into solution.

What is the basis for the relatively large temperature effect on k_d? Binding and dissociation of diatomic ligands such as NO, CO and O_2 to heme proteins is generally accompanied by conformational changes that sometimes extend far beyond the local heme-binding site [61 63]. This is a consequence of the disparate geometric, electronic and electrostatic requirements imposed by ligand binding and dissociation. The local and global conformational changes and dynamic electrostatic interactions in the binding pocket modulate not only ligand affinities, but also the discrimination between similar diatomic ligands [64,65]. The large temperature dependence of the observed rate of NO dissociation from ferric heme in nNOS and other heme proteins may reflect the control of NO binding at multiple levels. At the heme level, heme distortions have been shown to be critical for stabilizing the Fe^{III}NO complex, particularly in heme proteins whose physiological functions depend on controlling NO release from Fe^{III}-heme [63]. In NOS proteins, the observed out-of-plane modes in the low frequency regions of Raman spectra of the Fe^{III}NO species (oxygenase domain of the inducible nitric oxide synthase and oxygenase domain of the endothelial nitric oxide syn-

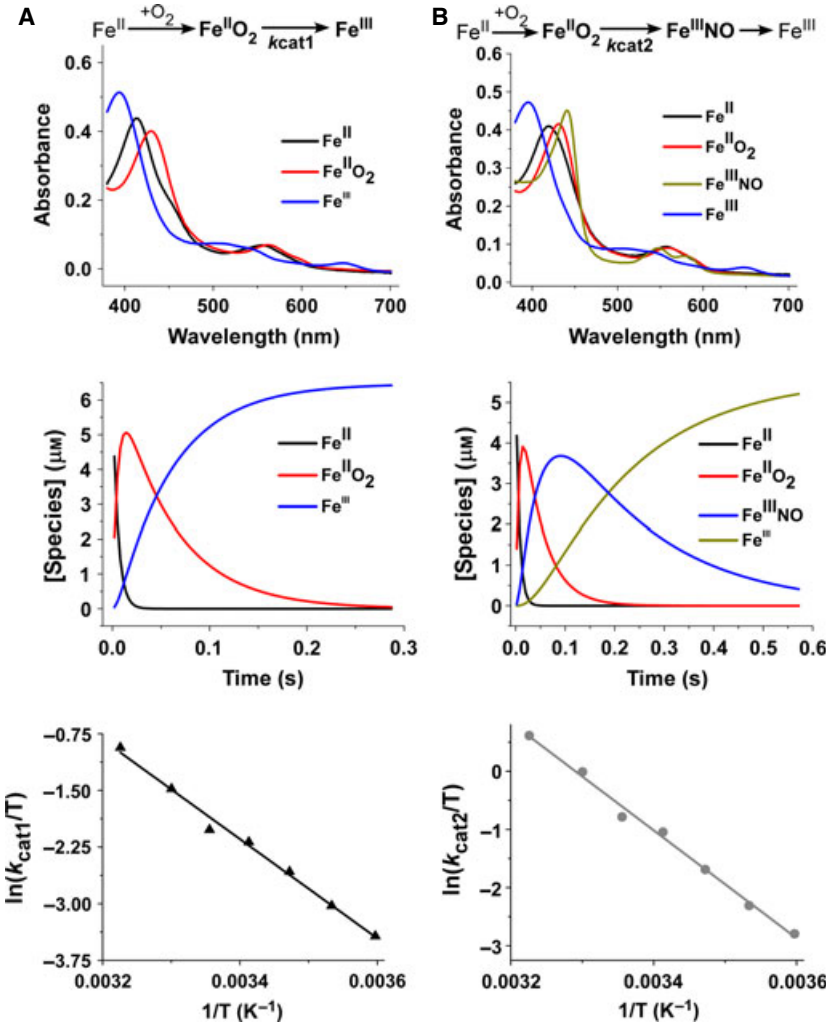

Fig. 3. Temperature dependence of the Arg and NOHA oxidation reactions (A, k_{cat1}; B, k_{cat2}) measured by single catalytic turnover reactions. Ferrous nNOSoxy containing H_4B and either Arg or NOHA was mixed at various temperatures with air saturated buffer in the stopped flow apparatus and diode array spectral data were collected. The transitions representing k_{cat1} and k_{cat2} are indicated. Upper panels: the spectrum of each heme species that was detected during each reaction as calculated by global analysis. Middle panels: the concentration versus time profiles for each heme species detected in each reaction. Lower panels: Eyring plots [ln(k_{cat}/T) versus 1/T] for the k_{cat1} and k_{cat2} transitions.

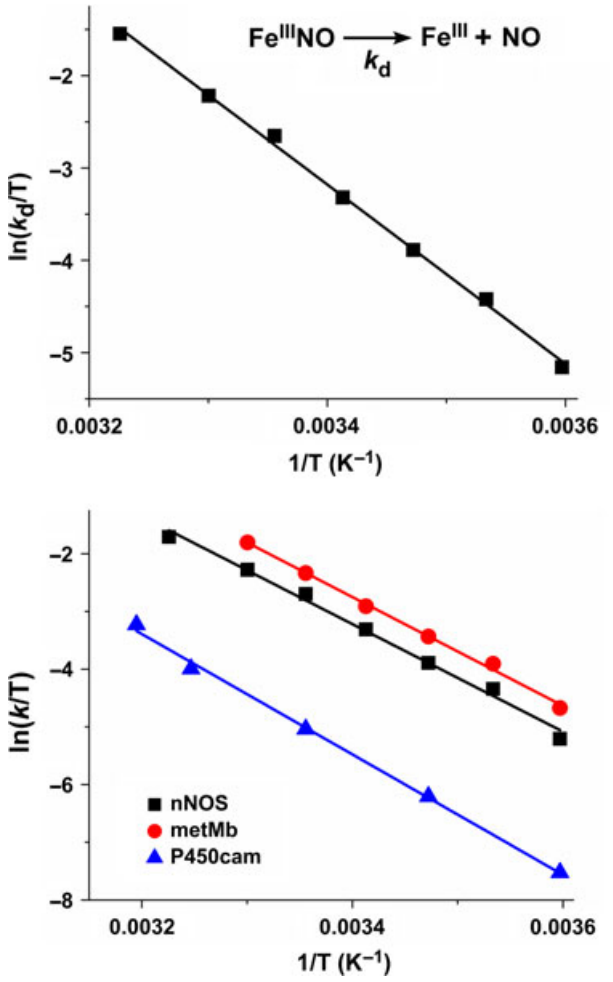

Fig. 4. Temperature dependence of NO release (k_d) from the $Fe^{III}NO$ product complex of nNOS. NOHA single turnover reactions were run with nNOSoxy at different temperatures, as described in Fig. 3. Upper panel: Eyring plot of measured NO release rates that were determined from the indicated spectral transition. Lower panel: Eyring plots of the NO release rates of nNOS (present study), metmyoglobin [59] and cytochrome P450cam proteins [60].

thase) have been assigned to heme distortions and have been shown to be critical in increasing d_{xy}-$d\pi$ orbital overlap, which stabilizes the $Fe^{III}NO$ species [62]. At the global protein level, it has been suggested that inter-subunit interactions in the NOS dimer may be important in modulating heme distortion modes [62], which in turn would affect the heme NO dissociation rate k_d. Also, point mutagenesis studies on NOS enzymes identified amino acids near the opening of the heme pocket that help to kinetically gate release of NO [25,66,67]. Thus, the large dependence of k_d on the temperature is likely a result of a general temperature effect on both the heme and protein structural fluctuations and dynamics.

Reaction of O_2 with the enzyme $Fe^{II}NO$ complex (k_{ox})

During NO synthesis a portion of the $Fe^{III}NO$ product complex is reduced by the NOS reductase domain and the resulting $Fe^{II}NO$ complex must then react with O_2 to return to the catalytic cycle. The rate of this reaction, termed k_{ox}, is a kinetic parameter (Fig. 1) that impacts NOS enzyme distribution during catalysis and, consequently, its steady-state behaviour and NO synthesis activity [19,68 70]. We determined k_{ox} values by mixing anaerobic samples of the nNOSoxy $Fe^{II}NO$ species with an air-saturated solution in the stopped-flow spectrophotometer at 5, 10, 15, 20, 25, 30 and 37 °C and then monitoring the reactions using a diode array detector. Figure 5 (upper panel) shows representative spectral data collected during the reaction of the nNOSoxy $Fe^{II}NO$ complex with air-saturated buffer in the presence of both H_4B and L-Arg at 10 °C. The spectral changes are consistent with conversion of the $Fe^{II}NO$ complex into the Fe^{III} high-spin form of nNOSoxy. The reaction was a single-step process with no discernible accumulation of intermediate species, as indicated by the several isosbestic points in the spectra (Fig. 5, upper panel) and by the single-exponential decay of the absorbance signal at two different wavelengths (Fig. 5, upper panel inset), which followed the rate of $Fe^{II}NO$ complex disappearance (436 nm) and the rate of ferric enzyme formation (393 nm). The spectral and fitting results obtained for reactions run at other temperatures were highly similar (data not shown) and the observed k_{ox} rates are listed in Table 1. The corresponding Eyring plot (Fig. 5, lower panel) and Arrhenius equation were used to calculate the thermodynamic parameters: E_a = 31.9 kJ·mol^{-1}; $\Delta H^{\ddagger}$ = 29.4 kJ·mol^{-1}; $\Delta S^{\ddagger} = -161$ J·mol^{-1}·K^{-1}) (Table 2).

The activation enthalpy for oxidation of the nNOS ferrous heme complex is much lower than the values reported for oxidation of ferrous heme-nitrosyl haemoglobin and myoglobin or for their various mutants ($\Delta H^{\ddagger}$ = 110 120 kJ·mol^{-1}) [61,71]. Their higher activation enthalpies have been rationalized in terms of a rate-limiting NO dissociation step governing the kinetics of the reversible ligand exchange reaction with O_2 that precedes the irreversible oxidation [71]. By contrast, the relatively low $\Delta H^{\ddagger}$ (29.4 kJ·mol^{-1}) that we measured for oxidation of the nNOS ferrous heme-nitrosyl species effectively argues against a NO dissociative mechanism being involved in this case because it is insufficient for breaking the strong heme-$Fe^{II}NO$ bond. The relatively low activation barrier for the nNOS reaction supports our recent mechanistic investigation of nNOS and iNOS heme-nitrosyl oxidation

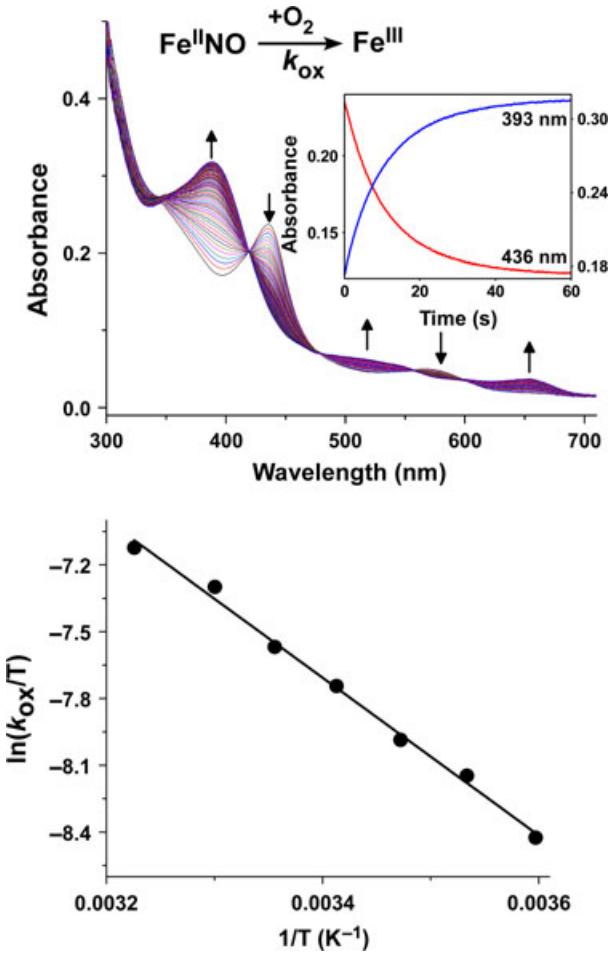

Fig. 5. Temperature dependence of the O_2 reaction with the $Fe^{II}NO$ species (k_{ox}). Anaerobic $Fe^{II}NO$ nNOSoxy was reacted at various temperatures with air saturated buffer in the stopped flow instrument. Upper panel: rapid scanning spectra recorded during a representative reaction, with arrows indicating the direction of the absorbance changes. Inset: absorbance changes versus time at 436 nm ($Fe^{II}NO$ disappearance) and 393 nm (Fe^{III} build up). Lower panel: Eyring plot of the measured k_{ox} values.

reactions, suggesting that it involves a comparatively fast and direct reaction between the ferrous heme-nitrosyl and dioxygen [24].

Steady-state NO synthesis activity

The steady-state NO synthesis activity is a combined reflection of all the individual steps in Fig. 1; thus, its temperature dependence provides apparent thermodynamic parameters for the global process. Table 1 contains NO synthesis activities that we measured across the temperature range for the present study (5 37 °C). The activity increased by approximately 12-fold over this range. The activity data gave a linear Eyring plot (Fig. 6), from which we determined the activation parameters: E_a = 54.1 kJ·mol^{-1}; $\Delta H^{\ddagger}$ = 51.7 kJ·mol^{-1}; $\Delta S^{\ddagger}$ = −74 J·mol^{-1}·K^{-1} (Table 2). Our E_a value differs somewhat from an earlier study that reported an activation energy of 79.4 kJ·mol^{-1} for the steady-state activity of nNOS, which was derived using measures of citrulline formation from [^{14}C]L-Arg [58].

Implications for nNOS catalytic behaviour

Because the five kinetic parameters investigated in the present study differed with respect to their temperature dependencies, this means that the distribution pattern of nNOS enzyme species during steady-state NO synthesis, and thus nNOS catalytic behaviours, will be temperature-dependent. We utilized the kinetic values that we measured for the five parameters at three different temperatures (10, 25 and 37 °C) in computer simulations of the global kinetic model (Fig. 1) [21] to explore this concept. The model reports on the five main enzyme species that are present during steady-state NO synthesis, namely the ferric, ferrous, ferrous-O_2 (or ferric-superoxy), ferric-NO and ferrous-NO forms (Fig. 1). Any additional kinetic values for associated reactions (i.e. O_2 binding) that we needed for the simulations, besides the five kinetic parameters measured in the present study, are described in the Experimental procedures.

At 10 °C, the simulation showed that the fast k_r relative to the slower k_d and k_{ox} values causes the nNOS

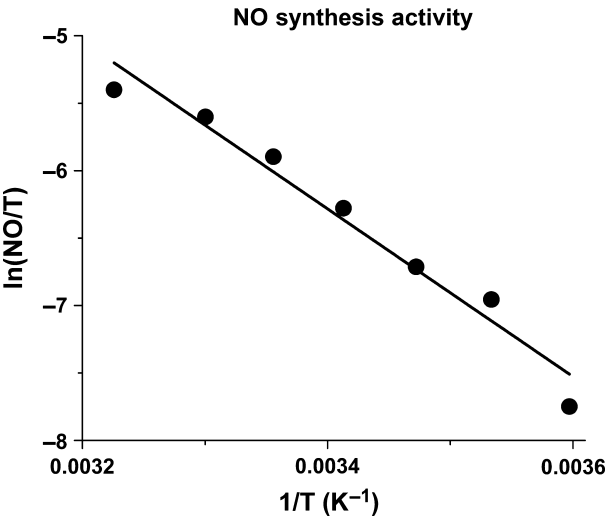

Fig. 6. Eyring plot of nNOS steady state NO synthesis activities recorded at different temperatures. Activities were measured in a conventional spectrophotometer using the oxyhaemoglobin assay for NO as described in the Experimental procedures. On Y axis, NO means Steady state NO synthesis rate.

enzyme to exist predominantly as the $Fe^{II}NO$ species during the steady-state [19,21]. The modelled enzyme distribution indicated that approximately 10% of nNOS is present as ferric enzyme and approximately 86% is present as the $Fe^{II}NO$ species (Fig. 7) at 10 °C, with the remaining 4% of nNOS mainly distributed between the $Fe^{II}O_2$ and $Fe^{III}NO$ species. This falls close to estimates reported in literature [16,19,21,72,73], which range between 67% and 85% $Fe^{II}NO$ complex during steady-state catalysis at 10 °C. However, our experimental data reveal that, at higher temperatures, the rate of $Fe^{III}NO$ dissociation (k_d) increases significantly faster than the k_r and the other kinetic parameters. The simulations indicate how this will alter the steady-state enzyme distributions: At 25 °C, approximately 16% of nNOS is present as ferric enzyme and approximately 81% is present as the $Fe^{II}NO$ species (Fig. 7), with the remaining 3% of nNOS mainly distributed between the $Fe^{II}O_2$ and $Fe^{III}NO$ species, whereas, at 37 °C, which is near the physiological temperature of rats (38 °C) [74,75], only approximately 73% of nNOS is present as the $Fe^{II}NO$ species and approximately 24% is present as ferric enzyme. These simulations clearly show that rat nNOS gains in ferric character and has less $Fe^{II}NO$ complex build-up during NO synthesis as the temperature increases. Overall, the different thermodynamic behaviours of the individual kinetic steps will cause nNOS to become more and more efficient at NO release as the temperature increases, at the same time as diminishing the enzyme cycling into the futile NO dioxygenase pathway (Fig. 1).

A related consequence of the different temperature dependencies is that the relative contributions of the individual kinetic steps toward limiting the NO synthesis activity, and in determining the catalytic behaviours of the enzyme, will change with temperature. For example, at low temperatures (e.g. 10 °C), the k_d and k_r have similar magnitudes. This equivalence diminishes the release of NO as a result of approximately half of the $Fe^{III}NO$ product complex being diverted into the futile cycle. Consequently, this increases the impact of k_{ox} on the observed enzyme NO synthesis activity and on its apparent oxygen concentration dependence (i.e. apparent K_mO_2). Specifically, NO synthesis activity becomes much more dependent on the oxygen concentration relationship of the NO dioxygenase reaction described by k_{ox} [72], which displays a linear relationship with O_2 concentration across the entire physiological range [24]. However, at higher temperatures, the k_d becomes increasingly faster than the k_r, which enables a quicker and greater release of NO from the $Fe^{III}NO$ product complex, consequently diminishing enzyme partitioning into the futile cycle. This in turn diminishes the role of k_{ox} in limiting the overall NO synthesis activity and diminishes its role in determining the apparent K_mO_2 for NO synthesis activity, such that the apparent K_mO_2 becomes more reflective of the oxygen concentration dependence of the biosynthetic reactions, which depend on the ferrous heme affinity for O_2 binding. Thus, at higher temperatures (i.e. 37 °C) the contribution of k_r in determining the overall NO synthesis activity is increased, whereas the contribution of k_{ox} is diminished, with accompanying changes in nNOS enzyme behaviour and the O_2 concentration response.

Experimental procedures

General methods and materials

All reagents and materials were obtained from Sigma Aldrich (St Louis, MO, USA), Amersham Biosciences

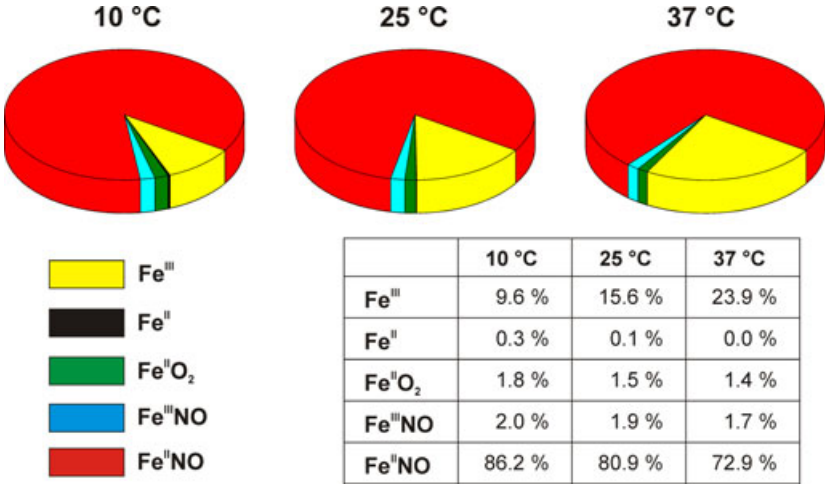

	10 °C	25 °C	37 °C
Fe^{III}	9.6 %	15.6 %	23.9 %
Fe^{II}	0.3 %	0.1 %	0.0 %
$Fe^{II}O_2$	1.8 %	1.5 %	1.4 %
$Fe^{III}NO$	2.0 %	1.9 %	1.7 %
$Fe^{II}NO$	86.2 %	80.9 %	72.9 %

Fig. 7. Temperature effect on the distribution of the five principal enzyme species during steady state NO synthesis by nNOS. Distributions were calculated by a computer simulating a global kinetic model similar to the one shown in Fig. 1. Rate constants used for the calculations are given in Table 3. Steady state values were determined after 50 s of simulated reaction, although a steady state distribution is reached within 5 10 s in all cases.

(Little Chalfont, UK) or other sources, as described previously [20,70,76]. Absorption spectra and steady state kinetic data were obtained using a Shimadzu UV 2401PC spectrophotometer (Shimadzu Corp., Kyoto, Japan). Stopped flow experiments were performed using a Hi Tech Scientific KinetAsyst SF 61DX2 stopped flow system (Hi Tech Scientific, Salisbury, UK) equipped with an anaerobic set up and a rapid scanning photodiode array detector. Data from multiple identical stopped flow experiments were averaged to improve the signal to noise ratio. We did not find much difference in values when individual rates were averaged or the rate was calculated from averaged trace. We calculated SD values from the individual observed rates. The spectral traces were fit according to single or multiple exponential equations using software provided by the manufacturer. The best fit was determined when adding further exponentials did not produce a significant improvement of the fit as judged from the residuals. All plots and some additional curve fitting were performed using ORIGIN, version 8.0 (OriginLab, Northampton, MA, USA). Anaerobic samples were prepared in an air tight cuvette using repeated cycles of vacuum followed by a positive pressure of catalyst deoxygenated nitrogen gas.

Expression and purification of wild-type protein

All proteins were purified in the presence of H_4B and L Arg as described previously [20,26,70,76]. The ferrous heme CO adduct absorbing at 444 nm was used to measure heme protein content with an extinction coefficient of $\varepsilon_{444} = 74\ mM^{-1}{\cdot}cm^{-1}$ (A_{444} A_{500}) [76]. The purity of each protein was assessed by SDS/PAGE and spectral analysis.

NO synthesis measurement

Steady state NO synthesis was determined at 5, 10, 15, 20, 25, 30 and 37 °C using the spectrophotometric oxyhaemoglobin assay, as described previously [76].

Anaerobic heme reduction measurements

The kinetics of heme reduction were analyzed at 5, 10, 15, 20, 25, 30 and 37 °C, as described previously [20,26,70,76,77], using a stopped flow apparatus and diode array detector (Hi Tech Scientific KinetAsyst SF 61DX2) equipped for anaerobic analysis.

Reaction of $Fe^{II}NO$ complexes with oxygen

The kinetics of $Fe^{II}NO$ oxidation were analyzed at 5, 10, 15, 20, 25, 30 and 37 °C, as described previously [24,70], using a stopped flow apparatus and diode array detector (Hi Tech Scientific KinetAsyst SF 61DX2) equipped for anaerobic analysis.

Single turnover reactions

Arginine hydroxylation experiments were carried out in a Hi Tech SF61 DX2 stopped flow instrument coupled to a diode array detector, as described previously [14]. The reactions were studied at 5, 10, 15, 20, 25, 30 and 37 °C in the presence of 50 μM H_4B, 2.5 mM L arginine, 150 mM NaCl, 10% glycerol, 1 mM dihiothreitol in 40 mM Epps buffer (pH 7.6). nNOSoxy at a concentration of 10 μM was titrated with sodium dithionite and mixed with air saturated buffer at the respective temperatures ($[O_2]$ = ~ 360 μM, 270 μM and 215 μM at 10, 25 and 37 °C, respectively). NOHA oxidation was studied in the same conditions replacing L arginine by 1 mM NOHA. Sequential spectral data were fitted to A→ B→ C (Arg hydroxylation; Fe^{II}→ $Fe^{II}O_2$→Fe^{III}) and A→ B→ C→ D (NOHA oxidation; Fe^{II}→ $Fe^{II}O_2$→$Fe^{III}NO$→Fe^{III}) kinetic models using SPECFIT/32 global analysis software, version 3.0 (Spectrum Software Associates, Marlborough, MA, USA) to obtain the spectra of the different species and the reaction rates. Using SPECFIT/32, we calculated rates for k_{cat1} (during Arg hydroxylation) and k_{cat2} (during NOHA oxidation).

Temperature-dependence and thermodynamic analysis

The natural log of the observed rates or rate constants for each averaged set of experimental data were plotted against the reciprocal of the absolute temperature. To calculate the activation energy, the data were then fit to the Arrhenius equation (Equation 3) using the linear fitting function in ORIGIN. In Equation (3), A is the Arrhenius pre exponential factor and R is the gas constant and E_a is activation energy. Activation enthalpy ($\Delta H^{\ddagger}$) and activation entropy ($\Delta S^{\ddagger}$) were calculated on the basis of Eyring equation (Equation 4) and Eyring plot [ln(k/T) versus 1/T]. Because the Gibbs free energy of activation ($\Delta G^{\ddagger}$) depends on temperature, it can be calculated for each step at a given temperature and we calculated $\Delta G^{\ddagger}$ at 25 °C using the Equation (5), whereas, $\Delta S^{\ddagger}$ and $\Delta H^{\ddagger}$ are virtually independent of temperature:

$$lnk \quad lnA \quad E_a/RT \tag{3}$$

$$ln(k/T) \quad \Delta H^{\ddagger}/RT + \Delta S^{\ddagger}/R + ln(k_B/h) \tag{4}$$

$$\Delta G^{\ddagger} \quad RT[ln(k_B T/h) \quad lnk] \tag{5}$$

where k is the reaction rate constant; T is the absolute temperature; R is the gas constant (8.314472 $J\ mol^{-1}{\cdot}K^{-1}$); k_B is the Boltzmann constant ($1.3806504 \times 10^{-23}\ J{\cdot}K^{-1}$); h is Planck's constant ($6.626 \times 10^{-34}\ J{\cdot}s^{-1}$); $\Delta H^{\ddagger}$ is the enthalpy of activation; $\Delta S^{\ddagger}$ is the entropy of activation; $\Delta G^{\ddagger}$ is the Gibbs free energy of activation; and E_a is the energy of activation.

Table 3. Calculated rates used for the computer simulations. (a) L Arg bound enzyme; (b) NOHA bound enzyme; (b*) ferric enzyme with NOHA and H_4B radical bound; for details, see Fig. 1 and Fig. S1. All values are in s^{-1}. For bimolecular reactions (k_2, k_6, k_{10}), the value used in the calculations is the product of the 'actual' value and the concentration of oxygen, which is considered to remain constant during the reaction. For k_2 and k_6, the values used are the experimental values multiplied by 2 (assumes the rate is proportional to $[O_2]$, experimental values are determined in half air saturated conditions). For k_{10}, the values used are the experimentally determined values × 1.5, as based on the observed oxygen dependence reported in Tejero *et al.* [24]. k_{11} values are interpolated from Salerno [17].

			Temperature						
			5 °C	10 °C	15 °C	20 °C	25 °C	30 °C	37 °C
k_1	$Fe^{III}a \rightarrow Fe^{II}(a)$	k_r	4.16	5.26	6.54	8.11	10.4	12.7	17.2
k_2	$Fe^{II}(a) (+ O_2) \rightarrow Fe^{II}O_2(a)$		56.8	115	228	438	826	1526	3488
k_3	$Fe^{II}O_2(a) \rightarrow Fe^{III}(b^*)$	k_{cat1}	9.2	13.5	20.6	31	46.1	67.7	113
k_4	$Fe^{III}(b^*) \rightarrow Fe^{III}(b)$	k_r'	4.16	5.26	6.54	8.11	10.4	12.7	17.2
k_5	$Fe^{III}(b) \rightarrow Fe^{II}(b)$	k_r''	4.16	5.26	6.54	8.11	10.4	12.7	17.2
k_6	$Fe^{II}(b) (+ O_2) \rightarrow Fe^{II}O_2(b)$		56.8	115	228	438	826	1526	3488
k_7	$Fe^{II}O_2(b) \rightarrow Fe^{III}NO$	k_{cat2}	16.4	28.7	52.2	92.9	162	278	572
k_8	$Fe^{III}NO \rightarrow Fe^{III}(a) + NO$	k_d	1.58	3.68	5.89	10.7	20.1	31.1	58.2
k_9	$Fe^{III}NO \rightarrow Fe^{II}NO$	k_r'''	4.16	5.26	6.54	8.11	10.4	12.7	17.2
k_{10}	$Fe^{II}NO (+ O_2) \rightarrow Fe^{III}(a) + NO_x$	k_{ox}	0.0948	0.121	0.153	0.191	0.233	0.31	0.381
k_{11}	$Fe^{II}NO \rightarrow Fe^{II}(a) + NO$		0.000052	0.000096	0.00018	0.00031	0.00054	0.00092	0.0019

Simulations of nNOS distribution during steady-state NO synthesis

The NO synthesis kinetics were simulated using the glo bal model as implemented in MATHCAD, version 7.0 [18,21] or GEPASI, version 3.30 [78]. Slight changes in the model were introduced to account for the pterin reduc tion step, as shown in Fig. 1. Both methods yielded simi lar results. Simulations assume constant values for $[O_2]$ = ~ 360 μM, 270 μM and 215 μM at 10, 25 and 37 °C, respectively, and [NADPH] = 40 μM. This approxi mation allows to treat all the processes as unimolecular reactions and assimilate the observed rates to apparent rate constants. Thus, for bimolecular reactions k_2, k_6 and k_{10} (Table 3), the observed rate is the product of the real rate constant multiplied by the concentration of oxygen. We base our simulations on the observed rates using a correction factor to estimate the value in air saturated buffer instead of the half air saturated experimental con ditions. Experimentally observed oxidation rates (k_{ox}), which we derived at half air saturated condition, were multiplied by a factor of 1.5 to approximate a full air saturated condition according to the dependence observed previously [24]. We also multiplied the observed oxygen binding rate k_2 and k_6 values by a factor of 2.0 to obtain a full air saturated condition assuming that the rate is proportional to $[O_2]$. The values for heme reduction (k_r), NO dissociation (k_d), $Fe^{II}NO$ oxidation (k_{ox}) and all other rates at different temperatures are shown in Table 3. The percentage of species in the steady state is calculated after 50 s of simulation, although a steady state distribution is reached within 5 10 s in all cases.

Acknowledgements

This work was supported by National Institutes of Health Grants GM51491 and HL58883 to D.J.S. We also acknowledge funding by The National Science Foundation to MB (Grant CHE-0848820).

References

1 Griffith OW & Stuehr DJ (1995) Nitric oxide synthases: properties and catalytic mechanism. *Annu Rev Physiol* **57**, 707 736.
2 Daff S (2010) NO synthase: structures and mechanisms. *Nitric Oxide* **23**, 1 11.
3 Alderton WK, Cooper CE & Knowles RG (2001) Nitric oxide synthases: structure, function and inhibition. *Biochem J* **357**, 593 615.
4 Gorren ACF, List BM, Schrammel A, Pitters E, Hemmens B, Werner ER, Schmidt K & Mayer B (1996) Tetrahydrobiopterin free neuronal nitric oxide synthase: evidence for two identical highly anticooperative pteridine binding sites. *Biochemistry* **35**, 16735 16745.
5 Wei CC, Crane BR & Stuehr DJ (2003) Tetrahydrobiopterin radical enzymology. *Chem Rev* **103**, 2365 2383.
6 Masters BS, McMillan K, Sheta EA, Nishimura JS, Roman LJ & Martasek P (1996) Neuronal nitric oxide synthase, a modular enzyme formed by convergent evolution: structure studies of a cysteine thiolate liganded heme protein that hydroxylates L arginine to produce NO• as a cellular signal. *FASEB J* **10**, 552 558.

7 Stuehr DJ (1997) Structure function aspects in the nitric oxide synthases. *Annu Rev Pharmacol Toxicol* **37**, 339 359.

8 Crane BR, Arvai AS, Ghosh DK, Wu C, Getzoff ED, Stuehr DJ & Tainer JA (1998) Structure of nitric oxide synthase oxygenase dimer with pterin and substrate. *Science* **279**, 2121 2126.

9 Fischmann TO, Hruza A, Niu XD, Fossetta JD, Lunn CA, Dolphin E, Prongay AJ, Reichert P, Lundell DJ, Narula SK *et al*. (1999) Structural characterization of nitric oxide synthase isoforms reveals striking active site conservation. *Nat Struct Biol* **6**, 233 242.

10 Gachhui R, Presta A, Bentley DF, Abu Soud HM, McArthur R, Brudvig G, Ghosh DK & Stuehr DJ (1996) Characterization of the reductase domain of rat neuronal nitric oxide synthase generated in the methylotrophic yeast *Pichia pastoris*. Calmodulin response is complete within the reductase domain itself. *J Biol Chem* **271**, 20594 20602.

11 Garcin ED, Bruns CM, Lloyd SJ, Hosfield DJ, Tiso M, Gachhui R, Stuehr DJ, Tainer JA & Getzoff ED (2004) Structural basis for isozyme specific regulation of electron transfer in nitric oxide synthase. *J Biol Chem* **279**, 37918 37927.

12 Sheta EA, McMillan K & Masters BS (1994) Evidence for a bidomain structure of constitutive cerebellar nitric oxide synthase. *J Biol Chem* **269**, 15147 15153.

13 Ledbetter AP, McMillan K, Roman LJ, Masters BS, Dawson JH & Sono M (1999) Low temperature stabilization and spectroscopic characterization of the dioxygen complex of the ferrous neuronal nitric oxide synthase oxygenase domain. *Biochemistry* **38**, 8014 8021.

14 Wang ZQ, Wei CC & Stuehr DJ (2002) A conserved tryptophan 457 modulates the kinetics and extent of N hydroxy L arginine oxidation by inducible nitric oxide synthase. *J Biol Chem* **277**, 12830 12837.

15 Wei CC, Wang ZQ, Wang Q, Meade AL, Hemann C, Hille R & Stuehr DJ (2001) Rapid kinetic studies link tetrahydrobiopterin radical formation to heme dioxy reduction and arginine hydroxylation in inducible nitric oxide synthase. *J Biol Chem* **276**, 315 319.

16 Abu Soud HM, Wang J, Rousseau DL, Fukuto JM, Ignarro LJ & Stuehr DJ (1995) Neuronal nitric oxide synthase self inactivates by forming a ferrous nitrosyl complex during aerobic catalysis. *J Biol Chem* **270**, 22997 23006.

17 Salerno JC (2008) Neuronal nitric oxide synthase: prototype for pulsed enzymology. *FEBS Lett* **582**, 1395 1399.

18 Santolini J, Meade AL & Stuehr DJ (2001) Differences in three kinetic parameters underpin the unique catalytic profiles of nitric oxide synthases I, II, and III. *J Biol Chem* **276**, 48887 48898.

19 Stuehr DJ, Santolini J, Wang ZQ, Wei CC & Adak S (2004) Update on mechanism and catalytic regulation in the NO synthases. *J Biol Chem* **279**, 36167 36170.

20 Haque MM, Panda K, Tejero J, Aulak KS, Fadlalla MA, Mustovich AT & Stuehr DJ (2007) A connecting hinge represses the activity of endothelial nitric oxide synthase. *Proc Natl Acad Sci USA* **104**, 9254 9259.

21 Santolini J, Adak S, Curran CM & Stuehr DJ (2001) A kinetic simulation model that describes catalysis and regulation in nitric oxide synthase. *J Biol Chem* **276**, 1233 1243.

22 Adak S, Bilwes AM, Panda K, Hosfield D, Aulak KS, McDonald JF, Tainer JA, Getzoff ED, Crane BR & Stuehr DJ (2002) Cloning, expression, and characterization of a nitric oxide synthase protein from Deinococcus radiodurans. *Proc Natl Acad Sci USA* **99**, 107 112.

23 Ray SS, Tejero J, Wang ZQ, Dutta T, Bhattacharjee A, Regulski M, Tully T, Ghosh S & Stuehr DJ (2007) Oxygenase domain of *Drosophila melanogaster* nitric oxide synthase: unique kinetic parameters enable a more efficient NO release. *Biochemistry* **46**, 11857 11864.

24 Tejero J, Santolini J & Stuehr DJ (2009) Fast ferrous heme NO oxidation in nitric oxide synthases. *FEBS J* **276**, 4505 4514.

25 Wang ZQ, Wei CC, Sharma M, Pant K, Crane BR & Stuehr DJ (2004) A conserved Val to Ile switch near the heme pocket of animal and bacterial nitric oxide synthases helps determine their distinct catalytic profiles. *J Biol Chem* **279**, 19018 19025.

26 Adak S, Aulak KS & Stuehr DJ (2001) Chimeras of nitric oxide synthase types I and III establish fundamental correlates between heme reduction, heme NO complex formation, and catalytic activity. *J Biol Chem* **276**, 23246 23252.

27 Li W, Chen L, Fan W & Feng C (2012) Comparing the temperature dependence of FMN to heme electron transfer in full length and truncated inducible nitric oxide synthase proteins. *FEBS Lett* **586**, 159 162.

28 Farver O & Pecht I (1989) Long range intramolecular electron transfer in azurins. *Proc Natl Acad Sci USA* **86**, 6968 6972.

29 Farver O, Einarsdottir O & Pecht I (2000) Electron transfer rates and equilibrium within cytochrome c oxidase. *Eur J Biochem* **267**, 950 954.

30 Farver O, Kroneck PM, Zumft WG & Pecht I (2002) Intramolecular electron transfer in cytochrome cd(1) nitrite reductase from *Pseudomonas stutzeri*; kinetics and thermodynamics. *Biophys Chem* **98**, 27 34.

31 Farver O, Brunori M, Cutruzzola F, Rinaldo S, Wherland S & Pecht I (2009) Intramolecular electron transfer in *Pseudomonas aeruginosa* cd(1) nitrite reductase: thermodynamics and kinetics. *Biophys J* **96**, 2849 2856.

32 Chien JC, Gibson HL & Dickinson LC (1978) Ferricytochrome c oxidation of cobaltocytochrome c. Comparison of experiments with electron transfer theories. *Biochemistry* **17**, 2579 2584.

33 Ivkovic Jensen MM & Kostic NM (1996) Effects of temperature on the kinetics of the gated electron transfer reaction between zinc cytochrome c and plastocyanin. Analysis of configurational fluctuation of the diprotein complex. *Biochemistry* **35**, 15095 15106.

34 King GC, Binstead RA & Wright PE (1985) NMR and kinetic characterization of the interaction between French bean plastocyanin and horse cytochrome c. *Biochim Biophys Acta* **806**, 262 271.

35 Marcus RA & Sutin N (1985) Electron transfers in chemistry and biology. *Biochim Biophys Acta* **811**, 265 322.

36 Davidson VL (2008) Protein control of true, gated, and coupled electron transfer reactions. *Acc Chem Res* **41**, 730 738.

37 Gray HB & Winkler JR (2010) Electron flow through metalloproteins. *Biochim Biophys Acta* **1797**, 1563 1572.

38 Ilagan RP, Tiso M, Konas DW, Hemann C, Durra D, Hille R & Stuehr DJ (2008) Differences in a conformational equilibrium distinguish catalysis by the endothelial and neuronal nitric oxide synthase flavoproteins. *J Biol Chem* **283**, 19603 19615.

39 Stuehr DJ, Tejero J & Haque MM (2009) Structural and mechanistic aspects of flavoproteins: electron transfer through the nitric oxide synthase flavoprotein domain. *FEBS J* **276**, 3959 3974.

40 Tejero J, Hannibal L, Mustovich A & Stuehr DJ (2010) Surface charges and regulation of FMN to heme electron transfer in nitric oxide synthase. *J Biol Chem* **285**, 27232 27240.

41 Xia C, Misra I, Iyanagi T & Kim JJ (2009) Regulation of interdomain interactions by calmodulin in inducible nitric oxide synthase. *J Biol Chem* **284**, 30708 30717.

42 Kobayashi K, Tagawa S, Daff S, Sagami I & Shimizu T (2001) Rapid calmodulin dependent interdomain electron transfer in neuronal nitric oxide synthase measured by pulse radiolysis. *J Biol Chem* **276**, 39864 39871.

43 Gao YT, Smith SM, Weinberg JB, Montgomery HJ, Newman E, Guillemette JG, Ghosh DK, Roman LJ, Martasek P & Salerno JC (2004) Thermodynamics of oxidation reduction reactions in mammalian nitric oxide synthase isoforms. *J Biol Chem* **279**, 18759 18766.

44 Noble MA, Munro AW, Rivers SL, Robledo L, Daff SN, Yellowlees LJ, Shimizu T, Sagami I, Guillemette JG & Chapman SK (1999) Potentiometric analysis of the flavin cofactors of neuronal nitric oxide synthase. *Biochemistry* **38**, 16413 16418.

45 Ost TW & Daff S (2005) Thermodynamic and kinetic analysis of the nitrosyl, carbonyl, and dioxy heme complexes of neuronal nitric oxide synthase. The roles of substrate and tetrahydrobiopterin in oxygen activation. *J Biol Chem* **280**, 965 973.

46 Presta A, Weber Main AM, Stankovich MT & Stuehr D (1998) Comparative effects of substrates and pterin cofactor on the heme midpoint potential in inducible and neuronal nitric oxide synthases. *J Am Chem Soc* **120**, 9460 9465.

47 Ilagan RP, Tejero J, Aulak KS, Ray SS, Hemann C, Wang ZQ, Gangoda M, Zweier JL & Stuehr DJ (2009) Regulation of FMN subdomain interactions and function in neuronal nitric oxide synthase. *Biochemistry* **48**, 3864 3876.

48 Salerno JC, Ray K, Poulos T, Li H & Ghosh DK (2013) Calmodulin activates neuronal nitric oxide synthase by enabling transitions between conformational states. *FEBS Lett* **587**, 44 47.

49 Harris TK, Davidson VL, Chen L, Mathews FS & Xia ZX (1994) Ionic strength dependence of the reaction between methanol dehydrogenase and cytochrome c 551i: evidence of conformationally coupled electron transfer. *Biochemistry* **33**, 12600 12608.

50 Wei CC, Wang ZQ, Tejero J, Yang YP, Hemann C, Hille R & Stuehr DJ (2008) Catalytic reduction of a tetrahydrobiopterin radical within nitric oxide synthase. *J Biol Chem* **283**, 11734 11742.

51 Astashkin AV, Elmore BO, Fan W, Guillemette JG & Feng C (2010) Pulsed EPR determination of the distance between heme iron and FMN centers in a human inducible nitric oxide synthase. *J Am Chem Soc* **132**, 12059 12067.

52 Sevrioukova IF, Hazzard JT, Tollin G & Poulos TL (1999) The FMN to heme electron transfer in cytochrome P450BM 3. Effect of chemical modification of cysteines engineered at the FMN heme domain interaction site. *J Biol Chem* **274**, 36097 36106.

53 Tejero J, Biswas A, Wang ZQ, Page RC, Haque MM, Hemann C, Zweier JL, Misra S & Stuehr DJ (2008) Stabilization and characterization of a heme oxy reaction intermediate in inducible nitric oxide synthase. *J Biol Chem* **283**, 33498 33507.

54 Tejero J, Biswas A, Haque MM, Wang ZQ, Hemann C, Varnado CL, Novince Z, Hille R, Goodwin DC & Stuehr DJ (2011) Mesohaem substitution reveals how haem electronic properties can influence the kinetic and catalytic parameters of neuronal NO synthase. *Biochem J* **433**, 163 174.

55 Giroud C, Moreau M, Mattioli TA, Balland V, Boucher JL, Xu Li Y, Stuehr DJ & Santolini J (2010) Role of arginine guanidinium moiety in nitric oxide synthase mechanism of oxygen activation. *J Biol Chem* **285**, 7233 7245.

56 Boggs S, Huang L & Stuehr DJ (2000) Formation and reactions of the heme dioxygen intermediate in the first and second steps of nitric oxide synthesis as studied by

stopped flow spectroscopy under single turnover conditions. *Biochemistry* **39**, 2332 2339.
57 Feng C & Tollin G (2009) Regulation of interdomain electron transfer in the NOS output state for NO production. *Dalton Trans* **34**, 6692 6700.
58 Iwanaga T, Yamazaki T & Kominami S (1999) Kinetic studies on the successive reaction of neuronal nitric oxide synthase from L arginine to nitric oxide and L citrulline. *Biochemistry* **38**, 16629 16635.
59 Laverman LE, Wanat A, Oszajca J, Stochel G, Ford PC & van ER, (2001) Mechanistic studies on the reversible binding of nitric oxide to metmyoglobin. *J Am Chem Soc* **123**, 285 293.
60 Franke A, Stochel G, Jung C & van ER, (2004) Substrate binding favors enhanced NO binding to P450cam. *J Am Chem Soc* **126**, 4181 4191.
61 Ford PC (2004) Probing fundamental mechanisms of nitric oxide reactions with metal centers. *Pure Appl Chem* **76**, 335 350.
62 Li D, Stuehr DJ, Yeh SR & Rousseau DL (2004) Heme distortion modulated by ligand protein interactions in inducible nitric oxide synthase. *J Biol Chem* **279**, 26489 26499.
63 Walker FA (2005) Nitric oxide interaction with insect nitrophorins and thoughts on the electron configuration of the {FeNO}6 complex. *J Inorg Biochem* **99**, 216 236.
64 Jain R & Chan MK (2003) Mechanisms of ligand discrimination by heme proteins. *J Biol Inorg Chem* **8**, 1 11.
65 Sigfridsson E & Ryde U (2002) Theoretical study of the discrimination between O(2) and CO by myoglobin. *J Inorg Biochem* **91**, 101 115.
66 Wang ZQ, Wei CC & Stuehr DJ (2010) How does a valine residue that modulates heme NO binding kinetics in inducible NO synthase regulate enzyme catalysis? *J Inorg Biochem* **104**, 349 356.
67 Whited CA, Warren JJ, Lavoie KD, Weinert EE, Agapie T, Winkler JR & Gray HB (2012) Gating NO release from nitric oxide synthase. *J Am Chem Soc* **134**, 27 30.
68 Adak S, Wang Q & Stuehr DJ (2000) Molecular basis for hyperactivity in tryptophan 409 mutants of neuronal NO synthase. *J Biol Chem* **275**, 17434 17439.
69 Adak S & Stuehr DJ (2001) A proximal tryptophan in NO synthase controls activity by a novel mechanism. *J Inorg Biochem* **83**, 301 308.
70 Haque MM, Fadlalla M, Wang ZQ, Ray SS, Panda K & Stuehr DJ (2009) Neutralizing a surface charge on the FMN subdomain increases the activity of neuronal nitric oxide synthase by enhancing the oxygen reactivity of the enzyme heme nitric oxide complex. *J Biol Chem* **284**, 19237 19247.
71 Moller JKS & Skibsted LH (2004) Mechanism of nitrosylmyoglobin autoxidation: temperature and oxygen pressure effects on the two consecutive reactions. *Chem Eur J* **10**, 2291 2300.
72 Abu Soud HM, Rousseau DL & Stuehr DJ (1996) Nitric oxide binding to the heme of neuronal nitric oxide synthase links its activity to changes in oxygen tension. *J Biol Chem* **271**, 32515 32518.
73 Adak S, Crooks C, Wang Q, Crane BR, Tainer JA, Getzoff ED & Stuehr DJ (1999) Tryptophan 409 controls the activity of neuronal nitric oxide synthase by regulating nitric oxide feedback inhibition. *J Biol Chem* **274**, 26907 26911.
74 Briese E (1998) Normal body temperature of rats: the setpoint controversy. *Neurosci Biobehav Rev* **22**, 427 436.
75 Owens NC, Ootsuka Y, Kanosue K & McAllen RM (2002) Thermoregulatory control of sympathetic fibres supplying the rat's tail. *J Physiol* **543**, 849 858.
76 Panda K, Haque MM, Garcin Hosfield ED, Durra D, Getzoff ED & Stuehr DJ (2006) Surface charge interactions of the FMN module govern catalysis by nitric oxide synthase. *J Biol Chem* **281**, 36819 36827.
77 Adak S, Santolini J, Tikunova S, Wang Q, Johnson JD & Stuehr DJ (2001) Neuronal nitric oxide synthase mutant (Ser 1412 → Asp) demonstrates surprising connections between heme reduction, NO complex formation, and catalysis. *J Biol Chem* **276**, 1244 1252.
78 Mendes P (1997) Biochemistry by numbers: simulation of biochemical pathways with Gepasi 3. *Trends Biochem Sci* **22**, 361 363.

Supporting information

Additional supporting information may be found in the online version of this article at the publisher's web site:

Fig. S1. Global kinetic model for NOS.

Fig. S2. Analysis of the temperature dependence data of observed heme reduction rates for nNOS using the modified Marcus equation with distance dependence.